Nanoscale

PAPER

View Article Online
View Journal | View Issue

Cite this: *Nanoscale*, 2019, **11**, 20315

Plasmon–exciton systems with high quantum yield using deterministic aluminium nanostructures with rotational symmetries†

Landobasa Y. M. Tobing,[a] Muhammad Danang Birowosuto,[b] Kah Ee Fong,[a] Yuan Gao,[a] Jinchao Tong,[a] Fei Suo,[a] Cuong Dang,[a,b] Hilmi Volkan Demir[a] and Dao Hua Zhang*[a]

Received 31st July 2019,
Accepted 25th September 2019

DOI: 10.1039/c9nr06311k

rsc.li/nanoscale

The abundance and corrosion-resistant properties of aluminium, coupled with its compatibility to silicon processing make aluminium an excellent plasmonic material for light–matter interaction in the ultraviolet-visible spectrum. We investigate the interplay of the excitation and emission enhancements of quantum dots coupled with ultra-small aluminium nanoantennae with varying rotational symmetries, where emission enhancements of ~8 and ~6 times have been directly measured for gammadion and star-shaped structures. We observed spontaneous emission modification in the Al antenna with a C_6 symmetry and deduce a Purcell factor in the range of $68.01 < F_P < 118.25$ at plasmonic hotspots, corresponding to a modified quantum yield of >89% in the single antenna and near-unity quantum yield at the plasmonic hotspots. This finding brings us a step closer towards the realization of circularly polarized nanoemitters.

A. Introduction

The coupling of strongly confined electromagnetic fields with optically active materials has been widely studied in plasmonic nanostructures, with its applications in controlling spontaneous emission,[1–10] light absorption,[11,12] higher harmonics generation[13–17] and Raman scattering.[18–21] In particular, the significant photoluminescence (PL) enhancement of quantum dots coupled to plasmonic nanoantennae resulting from a high spatial overlap between a plasmonic field and quantum emitters has potential applications in bright and ultrafast single emitters.[22–25] This is due to the increase of the local density of optical states (LDOS) which gives rise to the spontaneous emission rate improvement known as the Purcell effect, in addition to the modified radiation pattern and polarization of the quantum dot emissions arising from the plasmon–exciton coupling.[26,27] For these reasons, most of the antenna-emitter studies were conducted in plasmonic systems with highly directional radiation such as in nanoparticles on metal systems (NPoM),[6,28–30] and plasmonic systems with strong polarization dependence.[31–35] In order to have a strong interaction between the cavity mode and the exciton, most of the studied plasmonic systems were based on synthesized nanoparticles (bottom-up approaches), which are known for their better crystallinity and lower damping loss compared to those fabricated by top-down approaches such as lithographic methods. Depending on the technical process, the metal nanoparticles can be synthesized into nanocubes, nanospheres and even into shapes exhibiting chirality.[36] However, despite these advantages, the plasmonic cavities realized through self-assembly processes are still limited in terms of their geometries and orientations, which hinders further studies of the light–matter interaction in plasmonic antennae with more unique geometries, such as the rotationally symmetric and chiral metal nanostructures.

In this work, we explore the light–matter interaction between colloidal quantum dots and aluminium nanostructures with different rotational symmetries. The role of rotational symmetry in optical nanoantenna arrays has been investigated in many applications, notably in manipulating circularly polarized lights, generating optical orbital momentum, and controlling the local phase of harmonic generation.[37–39] Coupling colloidal quantum dots with radial dielectric grating has been demonstrated for lasing with azimuthal polarization characteristics.[40] In the absence of mirror symmetry, these structures exhibit circular dichroism, which measures the

[a]*School of Electrical and Electronic Engineering, Nanyang Technological University, 50 Nanyang Avenue, S639798, Singapore. E-mail: edhzhang@ntu.edu.sg*
[b]*CNRS International NTU Thales Research Alliance (CINTRA), Research Techno Plaza, 50 Nanyang Drive, Border X Block, 637553, Singapore*

† Electronic supplementary information (ESI) available: 1. The dynamics of field localization in the gammadion and C_n structure, 2. characterization of CdSe/CdS colloidal quantum dots, 3. gammadion longitudinal and transverse resonance modes, 4. finite difference time domain simulations for C_n structures coupled with the CQD film. See DOI: 10.1039/c9nr06311k

differential optical response between left-handed and right-handed circularly polarized lights. Ultrasensitive detection of chiral biomolecules has been demonstrated by superchiral electromagnetic fields.[41] The use of chiral nanostructures as circularly polarized luminescence (CPL) sources is yet another interesting application.[42–44] Aluminium (Al) is not investigated as extensively as gold (Au) and silver (Ag) for light–matter interactions due to its much higher damping loss, surface oxidation,[45] and the technical challenges in Al nanoparticle synthesis.[46] Nevertheless, the Al plasma oscillation frequency in the deep ultraviolet range enables surface plasmon resonance in the UV-vis spectrum,[45,47] which serves as an excellent platform for light–matter interaction where both the emission and excitation can be enhanced. Another advantage of using aluminium lies in its abundance and corrosive-resistant properties which, together with its compatibility with silicon processing, open up avenues towards mass production and practical applications of plasmonics.[48,49]

Here, we present a detailed study of the PL enhancements (PLEs) of colloidal quantum dots (CQDs) coupled to rotationally symmetric Al antennae, namely the 4-fold rotationally symmetric gammadion and the n-fold rotationally symmetric star-shaped (C_n) structures. We investigate the interplay of emission and excitation enhancements when the rotational symmetry is varied and observe 8-fold and 6-fold PL enhancements for the gammadion and the C_n structures, respectively. We present the time-resolved PL measurements of Al nanoantennae of C_6 symmetry with a measured spatially averaged Purcell factor of ~1.88, corresponding to a Purcell factor of ~91.25 at the plasmonic hotspots and modified quantum yield of >89% in a single antenna. We further show that the modified quantum yield could reach near unity at the plasmonic hotspots when the field-weighted averaging is taken into account.

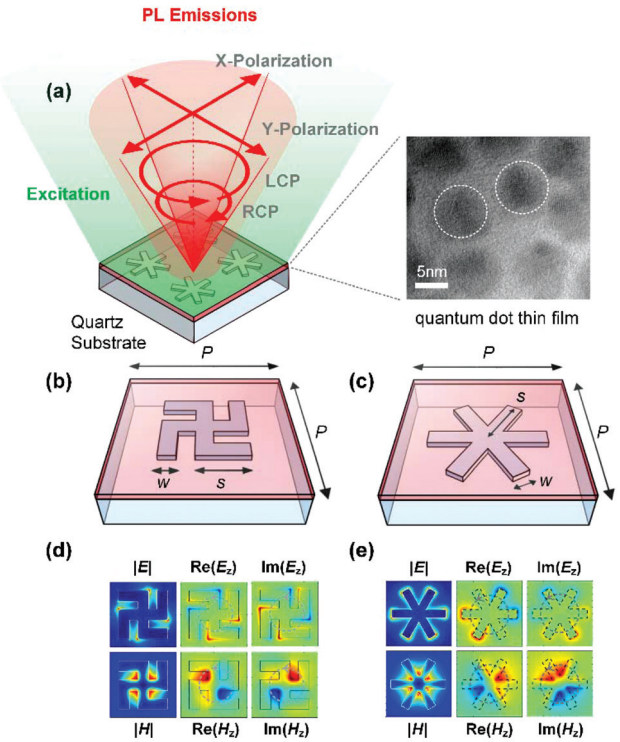

Fig. 1 (a) Illustration of the PL emissions of CQDs coupled with rotationally symmetric Al nanostructures, with the possible excitation of linearly polarized and circularly polarized modes. The CdSe/CdS nanocrystals are indicated by the dashed circles in the TEM image of the quantum dot thin film, with the estimated size of $d \sim 7.51 \pm 0.55$ nm. The schematic of (b) fourfold rotationally symmetric gammadion resonator and (c) a n-fold rotationally symmetric resonator (C_n), with $n = 6$. Electromagnetic field distribution at the fundamental resonance mode for (d) the gammadion ($s = 50$ nm) and (e) C_6 structure ($s = 70$ nm) under left circular polarized excitation (LCP, dashed grey circles).

B. Results and discussion

Resonance characteristics of gammadion and C_n structures

The photoluminescence of CQDs coupled with rotationally symmetric aluminium nanostructures is schematically illustrated in Fig. 1a, together with the transmission electron microscopy (TEM) image denoting the sub-10 nm CdSe/CdS nanocrystals. The resonance modes of the gammadion (Fig. 1b) and C_n antenna (Fig. 1c) have been analysed from the perspective of longitudinal plasmons, where the conductive coupling between longitudinal plasmons gives rise to the hybrid magnetic–electric resonance characteristics.[50] However, this type of mode analysis is based on linearly polarized excitation, which may not be adequate in the context of light–matter interaction as the mode excitation could originate from the quantum dot emission and/or the excitation source. Furthermore, the emissions from the colloidal quantum dots can be seen as uniformly distributed dipole sources of random orientations, without any correlation in phase. Therefore, in addition to the linearly polarized modes, there also exist circularly polarized modes associated with the superposition of linearly polarized modes in certain phase relations ($\Delta\varphi = \pm\pi/2$), suggesting that the plasmon-modulated emissions of CQD coupled with rotationally symmetric nanoantenna would have both the circular and linear polarization characteristics.

The circularly polarized modes in rotationally symmetric antennas are illustrated by full-wave simulations under left circularly polarized excitation (LCP, $\Delta\varphi = \pi/2$), as shown in Fig. 1d and e for the gammadion and C_n structures, respectively. The $|E|$ and $|H|$ fields describe the polarization invariance properties of the gammadion and C_n structures, while the complex E_z and H_z fields describe the dynamics of their circular polarization properties. The H_z field is mapped on the XY plane intersecting the resonator centre ($z = 0$), while the E_z field is intentionally mapped on the top surface of the resonators ($z = h/2$) to represent surface charge distributions associated with the electric dipole configuration of the resonance mode. As is evident from the complex field mappings, the field localizations do not occur simultaneously as in the $|E|$ and $|H|$ mappings, but rather in a cyclical fashion between the real and the imaginary field distributions. More comprehensive illustrations of the field localization dynamics are given in

the ESI Movies† for the gammadion and C_n structures under left circularly polarized (LCP) and right circularly polarized (RCP) excitation (ESI Note 1†).

Device fabrication

The rotationally symmetric Al nanostructures were realized by the nanofabrication method described in our previous work.[51] The Al nanostructures were fabricated on quartz substrates, followed by spin coating of a 40 nm thick quantum dot film. The reason for this thickness is to ensure a full coverage of the Al nanostructures, which are 30 nm in thickness. The native surface oxidation in the Al nanostructure (*i.e.*, ~3 nm thick) was also exploited to prevent emission quenching that typically occurs for the emitters in close contact with the metal. The PL spectra of the CQD film on a quartz substrate reveal an emission wavelength of λ_{em} = 615 nm, a full-width half-maximum of $\Delta\lambda_{cqd}$ = 56 nm, and a size distribution of the core–shell CdSe/CdS quantum dots of $d \sim 7.51 \pm 0.55$ nm based on 120 quantum dots (Fig. S1, ESI†). To compensate for the red shift caused by the Al interband loss, the Al nanostructures were fabricated at sub-100 nm sizes and sub-30 nm features, ensuring the resonance modes reside within the visible spectrum. For this reason, we fabricated a gammadion antenna with the armlength as small as s = 50 nm and star-shaped structures (C_n) of armlength s = 70 nm with the rotational symmetry varied from 3-fold (C_3) to 8-fold (C_8). Despite the presence of the e-beam proximity effects, the smallest fabricated structures still exhibit good pattern fidelities, as illustrated in Fig. 2a for the gammadion structure (s = 50 nm) and in Fig. 2b for the C_n structure (n = 5, s = 70 nm).

Transmission characteristics

The transmission measurements were carried out in a microscope system based on bright field geometry, where the sample is illuminated from the bottom by an unpolarized broadband halogen lamp focused through a condenser and the transmission signals are collected by 10× objective lens (NA = 0.3) into the hyperspectral imaging system (Cytoviva). The transmittance is then obtained by normalizing the transmitted signals of the Al nanoantenna with that of the substrate. The measured transmission spectra of gammadia with decreasing armlengths are presented in Fig. 2c. The periodicity (p) of the Al nanoantenna array is scaled according to the size (s) of the nanoantenna in order to improve the spectral contrast while minimizing the near-field coupling between the neighbouring resonators. Before CQD coating (solid curves), higher order modes at decreasing armlengths can be observed at ~618 nm (s = 100 nm), ~462 nm (s = 80 nm), ~435 nm (s = 60 nm) and ~447 nm (s = 50 nm). The slight red shift from s = 60 nm to s = 50 nm (instead of the expected blue shift) is attributed to the structural rounding caused by the e-beam proximity effects in the nanofabrication. This can be clearly seen in the SEM insets in Fig. 3c for gammadion with s = 60 nm and s = 50 nm.

The fundamental mode only starts to enter the visible spectrum at s = 60 nm, in the form of a broad resonance around 800 nm. This is the signature of the coupling between the plasmonic mode and the interband transition of Al ("IB", dashed blue line), which gives rise to resonance splitting around the IB transition.[51] The transmission spectra in the presence of quantum dots are shown as the dashed curves, which expectedly red shift due to the CQD coating. We also observed that the resonance mode for s = 50 nm appears much broader than

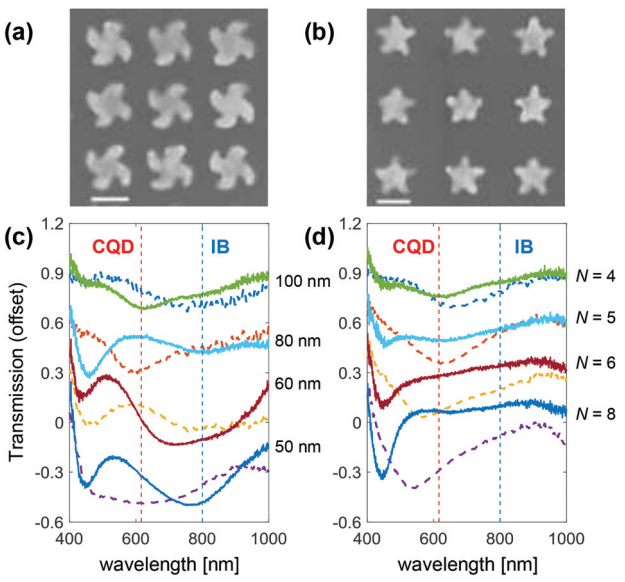

Fig. 2 The SEM micrographs of (a) gammadion with s = 50 nm, p = 175 nm, and (b) C_n with n = 5, s = 70 nm, p = 280 nm. The scale bars represent 100 nm. Transmission properties of (c) the gammadion (for different arm lengths) and (d) C_n structures (for different rotational symmetries) with colloidal quantum dots (dashed curves) and without colloidal quantum dots (solid curves). The locations of the emission wavelength of colloidal quantum dot and aluminium interband transmission are indicated by CQD and IB, respectively.

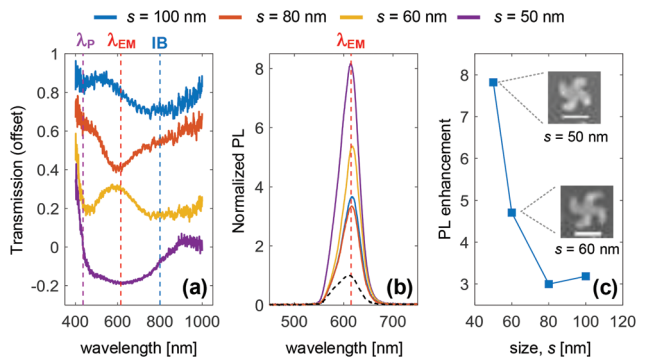

Fig. 3 PL enhancement in gammadion resonators. (a) Transmission, (b) normalized PL spectra, and (c) PL enhancements of Uf-SRR as the size (s) is decreased from s = 100 nm to s = 50 nm, with excitation (λ_P = 434 nm) and emission (λ_{EM} = 615 nm) wavelengths indicated by the dashed lines. The normalized PL intensity of CQDs on quartz is shown by the dashed curve in (b). (Insets) The fabricated gammadions with s = 60 nm and s = 50 nm at p = 3.5s periodicity. The scale bars represent 100 nm.

for other sizes, which is likely caused by a more pronounced material loss associated with the quantum dot excitation at the wavelength range shorter than the emission wavelength (*i.e.*, "CQD", dashed red line).

On the other hand, the transmission spectra of C_n structures with varying rotational symmetry are presented in Fig. 2d. The hybrid magnetic–electric resonance characteristics of C_n structures have been studied in terms of a superposition of the electric dipole resonances of its constituent nanorods, and the mode dependence on the number of arms has been analysed in terms of the transverse dipolar coupling between the nanorods.[50] We observed such an expected blue shift (resulting from transverse dipolar coupling) as the rotational symmetry increases from 4-fold to 8-fold, with the resonance mode positions at ~606 nm (n = 4), ~455 nm (n = 5), ~449 nm (n = 6) and ~443 nm (n = 8). Upon CQD coating (dashed curves), we observed that the resonance modes red shift to ~667 nm (n = 4), ~624 nm (n = 5), ~565 nm (n = 6) and ~535 nm (n = 8).

Photoluminescence enhancements

The photoluminescence measurements were carried out in the same microscope system based on dark field geometry, using 50× objective lens (NA = 0.55) and a mercury (Hg) lamp coupled with a 434 nm bandpass filter as the excitation source (λ_P = 434 nm). The dependence of the PL intensity on the excitation intensity (I_{EXC}), the emitter quantum yield (QY) and the extraction efficiency (η) indicates that the PLE can generally be described as $PLE(\Delta\lambda_P,\Delta\lambda_{em}) = PLE(I_{EXC},\Delta\lambda_P) \times PLE(I_{EM},\Delta\lambda_{em})$ for the detuning of the resonance mode from the emission ($\Delta\lambda_{em}$) and excitation ($\Delta\lambda_p$) sources. $PLE(I_{EXC},\Delta\lambda_P)$ describes the enhancement in the excitation intensity. $PLE(I_{EM},\Delta\lambda_{em}) = PLE(QY) \times PLE(\eta,\Delta\lambda_{em})$ describes the emission enhancement, which comprises the enhancement in the quantum yield PLE (QY) and the enhancement in the extraction efficiency PLE (η,$\Delta\lambda_{em}$), resulting respectively from the increase of the local density of states and the plasmon-induced radiation modification.

Fig. 3 shows the photoluminescence intensity enhancements of CQDs coupled with Al gammadia and their corresponding transmission characteristics. The PL signals of the CQD on the quartz substrate is denoted by the dashed curve in Fig. 3b, with its amplitude normalized to unity. The distribution of the quantum dots across the sample is illustrated by the PL intensity mapping, where the quantum dots are uniformly distributed both in the substrate and nanostructure area (Fig. S2†). The higher order mode shifts from ~800 nm to ~600 nm as the gammadion size decreases from s = 100 nm to s = 80 nm, yet the enhancement decreases from PLE ~ 3.2 to PLE ~ 3 despite the closer spectral proximity of the higher order mode towards the quantum dot emission (*i.e.*, "λ_{EM}", dashed red line) for the s = 80 nm case. We attribute this to the interplay of excitation and emission enhancements caused by the longitudinal and transverse plasmon modes in Al nanostructures. The existence of transverse plasmon modes is possible only in aluminium due to its plasma oscillation frequency in the deep UV range. The complete electromagnetic field distribution of Al gammadion is given in the ESI (Fig. S3†), which shows that the $|E|$-field distribution of the transverse plasmon-based resonance mode is similar to that of the fundamental mode, with also comparable field enhancements. The transmission characteristics of gammadion structures with and without the CQD coating are also presented in Fig. S4.† The interplay of longitudinal and transverse plasmons in the magnetic resonance excitation in Al split ring resonators (SRR) has been investigated, where preferential excitation of transverse plasmons in the UV range was demonstrated as the limiting mechanism for the achievable fundamental magnetic resonance in Al SRRs.[51]

In the context of gammadion with s = 100 nm (blue curve, Fig. 3a), the transverse plasmon-based resonance mode can be observed in the weak transmission dip around ~434 nm, which also coincides with the excitation source (λ_P = 434 nm). Given that the higher order mode is still far from the quantum dot emission, the PL enhancement of PLE ~ 3.2 is mainly caused the enhancement of the excitation intensity *via* the transverse plasmon mode at ~434 nm, *i.e.*, $PLE(I_{EM}) \sim 1$ and $PLE(I_{EXC},\Delta\lambda_P \sim 0) \sim 3.2$. As the size is decreased to s = 80 nm (red curve, Fig. 3a), the transverse plasmon-based mode is no longer observable in the visible spectrum and the higher order mode blue shifts to ~600 nm ($\Delta\lambda_{em}$ = 15 nm). This corresponds to lower excitation enhancement, but with higher emission enhancement, translating to a slightly lower PL enhancement of $PLE = PLE(I_{EXC}) \times PLE(I_{EM}) \sim 3$.

Further decreasing the gammadion size moves the fundamental mode into the visible spectrum and the higher order mode to the blue-side of the visible spectrum. For a gammadion with s = 60 nm, the observed resonance modes are all based on longitudinal plasmons, with the fundamental and higher order modes at ~800 nm and ~458 nm, respectively. Given the far detuning of both modes from the quantum dot emission (yellow curve, Fig. 3a), we can approximate $PLE(I_{EM},\Delta\lambda_{em}$ = 185 nm) ~ 1 and estimate the excitation enhancement based on the higher order mode as $PLE(I_{EXC},\Delta\lambda_p$ = 24 nm) ~ 4.7. As the gammadion size decreases to s = 50 nm the PL enhancement increases further to $PLE = PLE(I_{EXC})$ $PLE(I_{EM}) \sim 7.8$. The corresponding transmission spectrum (purple curve, Fig. 3a) shows a broad transmission dip encompassing both the excitation source and quantum dot emission, indicating that both the excitation and the emission are enhanced by the same resonance mode.

Unlike the gammadion structures which have resonance modes originating from longitudinal and transverse plasmons, the resonance characteristics of the C_n structures are more straightforward in that their resonance mode positions are all located in the mid-visible spectrum with no interaction with the Al interband transition (Fig. 2d). For this reason, the spectral overlap of the single resonance mode with excitation and emission wavelengths is further investigated in Fig. 4 for C_n structures of different rotational symmetries based on λ_P = 434 nm (Fig. 4b) and λ_P = 532 nm (Fig. 4c) excitation. For the 532 nm excitation, we used a WITec system where a green laser

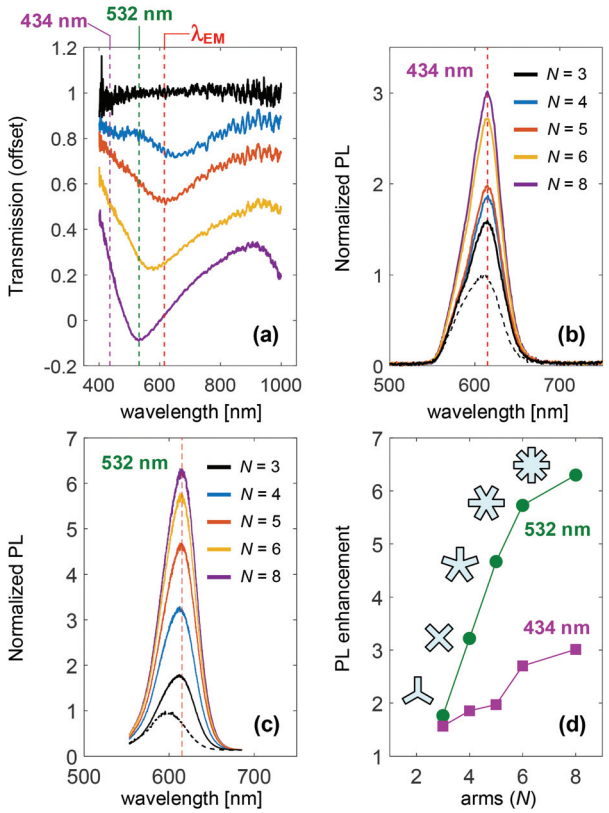

Fig. 4 The role of rotational symmetry in PL enhancement. (a) Transmission of C_n structures as N is increased from N = 3 to N = 8, (b) normalized PL spectra under 436 nm excitation, (c) normalized PL spectra under 532 nm excitation, (d) PL enhancements as a function of rotational symmetry at different excitation. The normalized PL intensities of CQD on quartz under 434 nm and 532 nm excitation are shown by the dashed curve in (b) and (c), respectively.

is focused onto Al nanostructures through 100× objective lens (~1 μm spot size) in the microscope system with a confocal geometry, from which the PL signals were delivered into a monochromator *via* optical fibre attached on top of the microscope. The PL enhancements for the increasing rotational symmetry under λ_P = 434 nm and λ_P = 532 nm excitation are presented in Fig. 4d, where a higher enhancement for λ_P = 532 nm is expected due to its closer spectral proximity to the resonance modes of the C_n structures. Table 1 summarizes the PL enhancements for all the C_n structures with their resonance full-width at half-maximum ($\Delta\lambda_{fwhm}$), emission detuning ($\Delta\lambda_{em}$), the 434 nm excitation detuning ($\Delta\lambda_{p1}$), the 532 nm detuning ($\Delta\lambda_{p2}$), and PLE_1 (PLE_2) denoting the PL enhancement under λ_P = 434 nm (λ_P = 532 nm) excitation. Since no resonance dip was observed in the experimental transmission spectra for the C_3 structure (n = 3), the $\Delta\lambda_{fwhm}$, $\Delta\lambda_{em}$, $\Delta\lambda_{p1}$, and $\Delta\lambda_{p2}$ were all obtained from numerical simulations instead (denoted by asterisks). The simulated transmission characteristics and the E-field distributions of all the C_n structures with the CQD film are given in the ESI (Fig. S5†). Nevertheless, PL enhancements of $PLE_1 \sim 1.56$ and $PLE_2 \sim 1.76$ are still observable despite the seemingly absent resonance mode in the C_3 transmission spectrum (Fig. 4a, black curve). It is also interesting that the PL enhancement for λ_P = 434 nm shows an increasing trend despite the fact that the emission detuning changes from $\Delta\lambda_{em}$ = 82 nm to $\Delta\lambda_{em}$ = −80 nm when the number of arms is increased from n = 3 to n = 8. Given that the 434 nm excitation source is sufficiently far from all the resonance modes, as indicated in Fig. 4a, we attribute this increasing trend to the larger scattering cross sections in C_n with a higher rotational symmetry.[50] This is also in agreement with the higher transmission contrast in the C_n structure with a higher rotational symmetry.

The interplay of the excitation and emission enhancements can be seen in situations with different resonance detuning and excitation wavelengths. The resonance mode for the C_4 structure is observed at ~667 nm ($\Delta\lambda_{em}$ = 52 nm), with PL enhancements of PLE_1 = 1.8 and PLE_2 = 3.2 corresponding to $\Delta\lambda_{p1}$ = 233 nm and $\Delta\lambda_{p2}$ = 135 nm excitation detunings. Following the same reasoning as in the gammadion case, as the 434 nm excitation source is far detuned from the resonance mode ($\Delta\lambda_p > \Delta\lambda_{fwhm}$), we approximate $PLE_1(I_{EXC},\Delta\lambda_p$ = 233 nm) ~ 1 and consequently deduce the emission enhancement as $PLE(I_{EM},\Delta\lambda_{em}$ = 52 nm) ~ 1.85. As the emission enhancement is not affected by the excitation detuning, the obtained emission enhancement can be used to deduce the excitation enhancement under 532 nm excitation, which is $PLE_2(I_{EXC},\Delta\lambda_{p2}) \cong PLE_2/PLE(I_{EM},\Delta\lambda_{em})$ = 1.74. An insight into the absorption efficiency of an excitation source can also be obtained from PL enhancements with similar excitation and emission detuning, namely the C_6 under 434 nm excitation ($\Delta\lambda_{em}$ = −50 nm,$\Delta\lambda_{p1}$ = 131 nm) and the C_4 under 532 nm excitation ($\Delta\lambda_{em}$ = 52 nm,$\Delta\lambda_{p2}$ = 135 nm). Comparison of their PL enhancements, *i.e.*, $PLE_2(C_4)/PLE_1(C_6)$ = 1.19, indicates that the 532 nm source is 19% more absorbed on the CQDs than the 434 nm source. We further show that the PL enhancement is dominated by the excitation enhancement, as evident from the situations associated with near zero emission detuning in the C_5 structure and near zero excitation detuning in the C_8 structure. The PL enhancements under 532 nm for these 2 cases are PLE_2 = 4.66 for $\Delta\lambda_{em}$ = 9 nm and $\Delta\lambda_{p2}$ = 92 nm (for C_5 structure, and PLE_2 = 6.3 for $\Delta\lambda_{em}$ = −80 nm and $\Delta\lambda_{p2}$ = 3 nm (for C_8 structure).

We then used fluorescence lifetime imaging to characterize the CQD emission decay rates for different scenarios shown in Fig. 5a, which shows the plot of the time-resolved PL signals of CQDs on quartz glass (black), CQDs on the Al metal film (blue) and CQDs coupled to Al C_6 structures (red). The distri-

Table 1 Photoluminescence intensity enhancements on Al C_n structures

N	$\Delta\lambda_{fwhm}$ (nm)	$\Delta\lambda_{em}$ (nm)	$\Delta\lambda_{p1}$ (nm)	$\Delta\lambda_{p2}$ (nm)	PLE_1	PLE_2
3	*117**	82*	263*	165	1.56	1.76
4	*221.66*	52	233	135	1.85	3.22
5	*250.23*	9	190	92	1.97	4.66
6	*231.34*	−50	131	33	2.70	5.73
8	*215.44*	−80	101	3	3.00	6.30

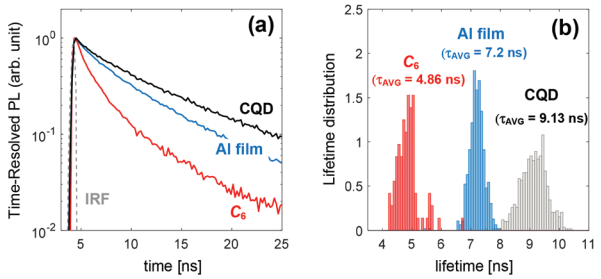

Fig. 5 Lifetime modification in Al rotationally symmetric nanostructures. (a) Time-resolved PL and (b) average lifetime distributions of the CQD substrate, CQD on the Al thin film, and CQD on C_6 Al nanostructures (s = 70 nm). The instrument response function (IRF) is denoted by the dashed curve.

bution of the emission lifetimes, deduced from single exponential curve fitting for each pixel, is presented in Fig. 5b, where the area under the curve for each distribution is normalized to unity. The clear modification in the emission lifetime can be observed as the CQDs (τ = 9.13 ± 0.45 ns) are coupled with the Al thin film (τ = 7.2 ± 0.26 ns) and Al C_6 structures (τ = 4.86 ± 0.39 ns). We ascertain that the faster CQD lifetime on the Al C_6 antenna is associated with the Purcell effect as the same Al C_6 structure also exhibits PL intensity enhancement under 434 nm and 532 nm excitation.

The single peak in the lifetime distribution indicates the polarization invariance characteristics of the Al C_6 structure, which differ qualitatively from the case of CQDs coupled to the Al dimer antenna with two distinct peaks in its lifetime distribution resulting from its polarization-resolved PL enhancements.[32] The Purcell effect refers to the spontaneous emission rate modification of quantum emitters coupled to an optical antenna due to the increase of the local density of states in the vicinity of the antenna.[52] The Purcell factor (F_P) has been shown to relate with the quantum yield by $F_P = (1 - QY)/(1 - QY')$, where QY′ and QY denote the quantum yields of the coupled and uncoupled CQDs, respectively.[53] The infinite Purcell factor $F_P = \infty$ thus corresponds to QY′ = 1 and the maximum quantum yield enhancement $PLE(QY)_{max} = 1/QY$ = 1.67 (QY = 0.6 for the CQDs used in this work). The spatially averaged Purcell factor for the Al C_6 structure is F_P^{avg} = 9.13/4.86 = 1.88, which corresponds to a modified average quantum yield QY'_{avg} = 0.79 and the average quantum yield enhancement PLE(QY) = 0.79/0.6 = 1.3.

The corresponding extraction efficiency enhancement can then be calculated by $PLE(\eta,\Delta\lambda_{em}) = PLE(I_{EM},\Delta\lambda_{em})/PLE(QY)$. However, as obtaining the emission enhancement is not possible for the C_6 structure because its resonance mode is detuned from both the emission and excitation, we use the previously estimated emission enhancement for the C_4 structure (under 434 nm excitation), whose emission detuning is similar to that of the C_6 structure (see Table 1). Using $PLE(I_{EM},\Delta\lambda_{em}$ = 52 nm) = 1.85 from the C_4 structure, the extraction efficiency enhancement for the C_6 structure is thus deduced as $PLE(\eta,\Delta\lambda_{em}) \cong 1.85/1.3 = 1.42$, indicating 42% higher extraction efficiency.

C. Discussions

We further estimate the Purcell factor for a single nanoantenna by noting that the experimentally measured Purcell factor is the local field-weighted average of the coupled and uncoupled quantum dots.[1,2,54] The fraction of the quantum dots coupled to the plasmonic hot spot is estimated by the fill factor $f = V_{mod}/(t_{na}p^2)$, where $V_{mod} = t_{na}\int_{cell} W dxdy/\max(W)$ is the mode volume at the CQD emission wavelength, $W = \frac{1}{2}\mathrm{Re}\{d[\omega\in(x,y)]/d\omega\}|E|^2 + \frac{1}{2}\mu_0|H|^2$ is the energy density, and t_{na} is the nanoantenna thickness. The experimental and best-fitted simulated transmittance of the C_6 Al nanoantenna coated with the 40 nm thick CQD film is presented in Fig. 6a, where the structural rounding due to e-beam proximity effects was taken into consideration in the fitting and the refractive index of the CQD film was obtained from ellipsometer measurements. In addition, the spectral contrast of the simulated transmittance was adjusted to match the experimental transmittance in order to take into account the off-normal mode excitations from other incident angles dictated by the numerical aperture of the condenser. The $|E|^2$ field distribution for the left circularly polarized mode at λ_{em} = 615 nm is presented in Fig. 6b. Based on the calculated $V_{mod} = 3.53 \times 10^{-4}(\lambda/n)^3$ and $f = 9.8 \times 10^{-3}$, we deduce the Purcell factor for a single antenna as F_P = 91.25, which is ~48.53 times higher than its spatially averaged experimental value.

The ideal Purcell factor is based on the assumption that the emitters are located at the plasmonic hotspot with their dipole

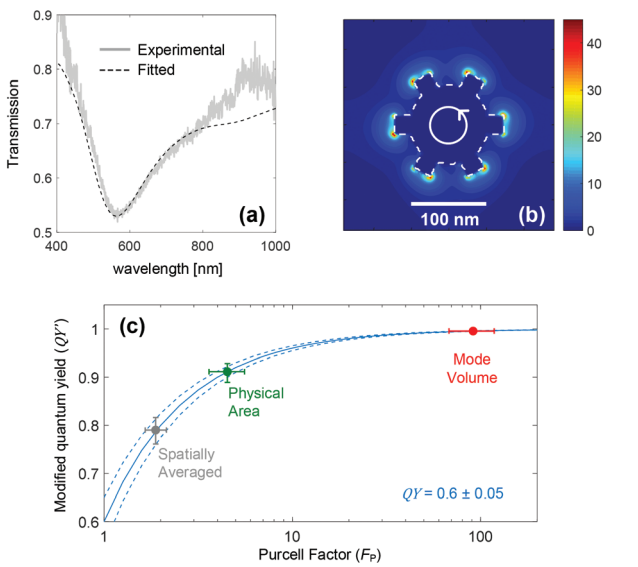

Fig. 6 (a) Experimental (solid) and simulated (dashed) transmission spectra of the C_6 Al nanoantenna. (b) $|E|^2$ field distribution of the left-handed polarized resonance mode at λ_{em} = 615 nm. (c) The projection of the modified quantum yield based on the spatially averaged experimental value, physical area of the C_6 nanoantenna, and mode volume of the plasmonic mode field in (b). The dashed curves illustrate the uncertainty in the quantum yield measurement, QY = 0.6 ± 0.05.

orientations in perfect alignment with the mode field. For a detuned cavity,[2] the theoretical Purcell factor is

$$F_{\mathrm{P,ideal}}(\omega) = \frac{3\lambda^3\omega}{4\pi^2 n^3 V_{\mathrm{mod}}} \frac{\Delta\omega_{\mathrm{cav}}}{4(\omega-\omega_{\mathrm{cav}})^2 + \Delta\omega_{\mathrm{cav}}{}^2} \quad (1)$$

which is found to be $F_{\mathrm{P,ideal}} = 435.73$ based on $|\omega_{\mathrm{em}} - \omega_{\mathrm{cav}}|/\Delta\omega_{\mathrm{cav}} = 0.21$ and $Q = \omega_{\mathrm{cav}}/\Delta\omega_{\mathrm{cav}} = 2.6$ for the C_6 Al antenna in Fig. 5. The theoretical Purcell factor is ~4.77 times higher than the estimated Purcell factor for a single antenna deduced from our time-resolved PL measurements. This is attributed mainly to the $\cos^2\theta$ dependence in the emission rate for a dipole at angle θ from the local E-field,[54] which can be estimated as $\theta = \cos^{-1}\left(\sqrt{F_{\mathrm{P}}/F_{\mathrm{P,ideal}}}\right) \sim 62°$. It is worth mentioning that the Purcell factor for the Al C_6 antenna is higher than that for the Al dimer, despite the stronger E-field enhancement across nanogaps and higher quality factor ($Q \sim 6.05$) in the latter.[32] This is because the mode volume of the Al dimer is $V_{\mathrm{mod}} = 2.1 \times 10^{-3}(\lambda/n)^3$, which is ~6× larger than that of the Al C_6 antenna, making the Al C_6 antenna exhibit ~2.5× higher Q/V_{mod} than the Al dimer. This is also reflected in the theoretical Purcell factor of the Al dimers $F_{\mathrm{P,Dimer}} = 104.9$,[32] which is ~4.15× smaller than the theoretical Purcell factors of the Al C_6 antenna. The modified quantum yield of CQDs coupled to a single antenna is then estimated based on upper and lower bounds of the Purcell factors derived from the standard deviations in the lifetime distributions in Fig. 5b, showing a Purcell factor in the range of $68.01 < F_{\mathrm{P}} < 118.25$ and modified quantum yield of near unity (see ESI Note 6† for the detailed calculations). The lower bound of the modified quantum yield for a single nanoantenna can be conservatively estimated based on the physical area of the nanoantenna instead of the mode volume. Using $A_{\mathrm{cav}} = 4s^2$ to represent the areal footprint of the C_6 nanoantenna and the fill ratio of $f = A_{\mathrm{cav}}/p^2 = 0.25$, a modified quantum yield of $\mathrm{QY}' > 0.89$ is obtained. The estimates based on physical area and mode volume, together with the experimentally measured Purcell factor, are mapped in relation to the modified quantum yield and the Purcell factor as shown in Fig. 6c, with the dashed curves representing ±0.05 uncertainty in the quantum yield measurement of the colloidal quantum dot.[55]

On the emission polarization characteristics, although both linearly and circularly polarized modes are supported in rotationally symmetric resonators, the polarization characteristics of our plasmon-modulated emission cannot be known due to some limitations in our experiments. However, specific polarization characteristics can be selectively enhanced by incorporating rotational symmetry and resonator orientation into the resonator lattice arrangements.[37] This could be an interesting future work, particularly in the context of realizing circularly polarized light sources.

D. Conclusions

Plasmon-induced emission enhancements of CdSe/CdS colloidal quantum dots coupled with Al gammadion and star-shaped nanostructures have been investigated, where PL intensity enhancements of ~8 and ~6 times have been experimentally measured. The interplay of the excitation and emission enhancements in the C_n structure for two different excitation sources has been studied, and the dependence of PL enhancement on the rotational symmetry has been indirectly observed under 434 nm excitation. Spontaneous emission rate modification has been observed in the time-resolved PL measurements of the Al C_6 antenna with a spatially averaged Purcell factor of ~1.88, corresponding to ~30% higher quantum yield and ~42% higher extraction efficiency. The modified quantum yield associated with a single antenna is estimated to be higher than 89%, and could potentially reach near unity when estimated based on the mode volume where only ~0.98% of quantum dots are within the mode volume. In terms of the Purcell factor, this corresponds to $68.01 < F_{\mathrm{P}} < 118.25$ at the plasmonic hotspots. Finally, although determining the polarization characteristics of the enhanced emissions is beyond the scope of this work, we note the possibility to selectively enhance certain polarization characteristics *via* introducing rotational symmetry and resonator orientation in the lattice arrangement, which is a step closer towards the realization of circularly polarized light sources.

Author contributions

LYMT conceived the idea, fabricated the Al nanostructures, and characterized the transmission and photoluminescence mapping properties of the plasmonic nanostructures. DHZ supervised the project. LYMT built the photoluminescence mapping setup. KEF synthesized and characterized the CdSe/CdS quantum dots. MDB, YG, CD, and HVD facilitated and characterized time-resolved photoluminescence. MDB and CD contributed technical discussions on photoluminescence and the Purcell factor. LYMT wrote the manuscript, with inputs from DHZ and all other authors. All authors read and approved the manuscript.

Conflicts of interest

There are no conflicts to declare.

Acknowledgements

This work is supported by the A*Star (SERC 1720700038 and SERC A1883c0002) and the Ministry of Education (2017-T1-002-117) Singapore, and the Asian Office of Aerospace Research and Development (FA2386-17-1-0039).

Notes and references

1 K. Tanaka, E. Plum, J. Y. Ou, T. Uchino and N. I. Zheludev, *Phys. Rev. Lett.*, 2010, **105**, 227403.

2 M. Decker, I. Staude, I. I. Shishkin, K. B. Samusev, P. Parkinson, V. K. A. Sreenivasan, A. Minovich, A. E. Miroshnichenko, A. Zvyagin, C. Jagadish, D. N. Neshev and Y. S. Kivshar, *Nat. Commun.*, 2013, **4**, 2949.
3 H. Hu, H. Duan, J. K. W. Yang and Z. X. Shen, *ACS Nano*, 2012, **6**, 10147–10155.
4 Z. Wang, Z. Dong, Y. Gu, Y.-H. Chang, L. Zhang, L.-J. Li, W. Zhao, G. Eda, W. Zhang, G. Grinblat, S. A. Maier, J. K. W. Yang, C.-W. Qiu and A. T. S. Wee, *Nat. Commun.*, 2016, **7**, 11283.
5 J. Huang, K. H. P. Tung, L. Deng, N. Xiang, J. Dong, A. J. Danner and J. Teng, *Opt. Mater. Express*, 2013, **3**, 2003.
6 A. Rose, T. B. Hoang, F. McGuire, J. J. Mock, C. Ciracì, D. R. Smith and M. H. Mikkelsen, *Nano Lett.*, 2014, **14**, 4797–4802.
7 T. T. Tran, D. Wang, Z.-Q. Xu, A. Yang, M. Toth, T. W. Odom and I. Aharonovich, *Nano Lett.*, 2017, **17**, 42.
8 J. N. Farahani, D. W. Pohl, H.-J. Eisler and B. Hecht, *Phys. Rev. Lett.*, 2005, **95**, 017402.
9 A. Kinkhabwala, Z. Yu, S. Fan, Y. Avlasevich, K. Müllen and W. E. Moerner, *Nat. Photonics*, 2009, **3**, 654–657.
10 Y. Luo and J. Zhao, *Nano Res.*, 2019, 1–8.
11 F.-F. Ren, K.-W. Ang, J. Ye, M. Yu, G.-Q. Lo and D.-L. Kwong, *Nano Lett.*, 2011, **11**, 46.
12 C.-C. C. Chang, Y. D. Sharma, Y.-S. S. Kim, J. A. Bur, R. V. Shenoi, S. Krishna, D. Huang and S.-Y. Y. Lin, *Nano Lett.*, 2010, **10**, 1704–1709.
13 V. K. Valev, B. D. Clercq, X. Zheng, D. Denkova, E. J. Osley, S. Vandendriessche, A. V. Silhanek, V. Volskiy, P. A. Warburton, G. A. E. Vandenbosch, M. Ameloot, V. V. Moshchalkov and T. Verbiest, *Opt. Express*, 2012, **20**, 256–264.
14 B. Metzger, T. Schumacher, M. Hentschel, M. Lippitz and H. Giessen, *ACS Photonics*, 2014, **1**, 471–476.
15 A. Slablab, L. Le Xuan, M. Zielinski, Y. de Wilde, V. Jacques, D. Chauvat and J.-F. Roch, *Opt. Express*, 2011, **20**, 6.
16 J. Butet, P.-F. Brevet and O. J. F. Martin, *ACS Nano*, 2015, **9**, 10545–10562.
17 G. Sartorello, N. Olivier, J. Zhang, W. Yue, D. J. Gosztola, G. P. Wiederrecht, G. Wurtz and A. V. Zayats, *ACS Photonics*, 2016, **3**, 1517–1522.
18 M. D. Doherty, A. Murphy, R. J. Pollard and P. Dawson, *Phys. Rev. X*, 2013, **3**, 1–12.
19 W. Yue, Y. Yang, Z. Wang, L. Chen and X. Wang, *J. Phys. Chem. C*, 2013, **117**, 21908–21915.
20 X. Wen, G. Li, J. Zhang, Q. Zhang, B. Peng, L. M. Wong, S. Wang and Q. Xiong, *Nanoscale*, 2014, **6**, 132–139.
21 A. W. Clark, A. Glidle, D. R. S. Cumming and J. M. Cooper, *J. Am. Chem. Soc.*, 2009, **131**, 17615–17619.
22 O. L. Muskens, V. Giannini, J. A. Sánchez-Gil, J. Gómez Rivas and J. A. Sa, *Nano Lett.*, 2007, **7**, 2871–2875.
23 T. B. Hoang, G. M. Akselrod, C. Argyropoulos, J. Huang, D. R. Smith and M. H. Mikkelsen, *Nat. Commun.*, 2015, **6**, 7788.
24 G. M. Akselrod, M. C. Weidman, Y. Li, C. Argyropoulos, W. A. Tisdale and M. H. Mikkelsen, *ACS Photonics*, 2016, **3**, 1741–1746.
25 T. B. Hoang, G. M. Akselrod and M. H. Mikkelsen, *Nano Lett.*, 2016, **16**, 270–275.
26 A. F. Koenderink, *Opt. Lett.*, 2010, **35**, 4208–4210.
27 G. Sun and J. B. Khurgin, *Phys. Rev. A*, 2012, **85**, 063410.
28 M.-E. Kleemann, R. Chikkaraddy, E. M. Alexeev, D. Kos, C. Carnegie, W. Deacon, A. C. de Pury, C. Große, B. de Nijs, J. Mertens, A. I. Tartakovskii and J. J. Baumberg, *Nat. Commun.*, 2017, **8**, 1296.
29 J. Huang, G. M. Akselrod, T. Ming, J. Kong and M. H. Mikkelsen, *ACS Photonics*, 2018, **5**, 552–558.
30 Y. Luo, G. D. Shepard, J. V. Ardelean, D. A. Rhodes, B. Kim, K. Barmak, J. C. Hone and S. Strauf, *Nat. Nanotechnol.*, 2018, 1.
31 T. Yin, Z. Dong, L. Jiang, L. Zhang, H. Hu, C.-W. Qiu, J. K. W. Yang and Z. X. Shen, *ACS Photonics*, 2016, **3**, 979–984.
32 L. Y. M. Tobing, D. H. Zhang, K. E. Fong, M. D. Birowosuto, Y. Gao, C. H. Dang and H. V. Demir, *ACS Photonics*, 2018, **5**, 1566–1574.
33 J. Kern, A. Trügler, I. Niehues, J. Ewering, R. Schmidt, R. Schneider, S. Najmaei, A. George, J. Zhang, J. Lou, U. Hohenester, S. Michaelis De Vasconcellos and R. Bratschitsch, *ACS Photonics*, 2015, **2**, 1260–1265.
34 S. Luo, Q. Li, Y. Yang, X. Chen, W. Wang, Y. Qu and M. Qiu, *Laser Photonics Rev.*, 2017, **11**, 1600299.
35 M. H. Tahersima, M. Danang Birowosuto, Z. Ma, W. C. Coley, M. D. Valentin, S. N. Alvillar, I.-H. Lu, Y. Zhou, I. Sarpkaya, A. Martinez, I. Liao, B. N. Davis, J. Martinez, D. Martinez-Ta, A. Guan, A. E. Nguyen, K. Liu, C. Soci, E. Reed, L. Bartels and V. J. Sorger, *ACS Photonics*, 2017, **4**, 1713–1721.
36 H.-E. Lee, H.-Y. Ahn, J. Mun, Y. Y. Lee, M. Kim, N. H. Cho, K. Chang, W. S. Kim, J. Rho and K. T. Nam, *Nature*, 2018, **556**, 360–365.
37 S. Chen, G. Li, K. Wai Cheah, T. Zentgraf and S. Zhang, *Nanophotonics*, 2018, **7**, 1013–1024.
38 M. Kuwata-Gonokami, N. Saito, Y. Ino, M. Kauranen, K. Jefimovs, T. Vallius, J. Turunen and Y. Svirko, *Phys. Rev. Lett.*, 2005, **95**, 1–4.
39 M. Hentschel, M. Schäferling, X. Duan, H. Giessen and N. Liu, *Sci. Adv.*, 2017, **3**, e1602735.
40 Y. Gao, L. Y. M. Tobing, A. Kiffer, D. H. Zhang, C. Dang and H. V. Demir, *ACS Photonics*, 2016, **3**, 2255–2261.
41 E. Hendry, T. Carpy, J. Johnston, M. Popland, R. V. Mikhaylovskiy, A. J. Lapthorn, S. M. Kelly, L. D. Barron, N. Gadegaard and M. Kadodwala, *Nat. Nanotechnol.*, 2010, **5**, 783–787.
42 K. Q. Le, S. Hashiyada, M. Kondo and H. Okamoto, *J. Phys. Chem. C*, 2018, **122**, 24924–24932.
43 K. Konishi, M. Nomura, N. Kumagai, S. Iwamoto, Y. Arakawa and M. Kuwata-Gonokami, *Phys. Rev. Lett.*, 2011, **106**, 057402.

44 C. Yan, X. Wang, T. V. Raziman and O. J. F. Martin, *Nano Lett.*, 2017, **17**, 2265–2272.
45 M. W. Knight, N. S. King, L. Liu, H. O. Everitt, P. Nordlander and N. J. Halas, *ACS Nano*, 2014, **8**, 834–840.
46 G. Maidecchi, G. Gonella, R. Proietti Zaccaria, R. Moroni, L. Anghinolfi, A. Giglia, S. Nannarone, L. Mattera, H.-L. Dai, M. Canepa and F. Bisio, *ACS Nano*, 2013, **7**, 5834–5841.
47 M. W. Knight, L. Liu, Y. Wang, L. Brown, S. Mukherjee, N. S. King, H. O. Everitt, P. Nordlander and N. J. Halas, *Nano Lett.*, 2012, **12**, 6000–6004.
48 D. Gérard and S. K. Gray, *J. Phys. D: Appl. Phys.*, 2015, **48**, 184001.
49 A. Moscatelli, *Nat. Nanotechnol.*, 2012, **7**, 778–778.
50 L. Y. M. Tobing, G.-Y. Goh, A. D. Mueller, L. Ke, Y. Luo and D.-H. Zhang, *Sci. Rep.*, 2017, **7**, 7539.
51 L. Y. M. Tobing and D.-H. Zhang, *Adv. Mater.*, 2016, **28**, 889–896.
52 E. M. Purcell, H. C. Torrey and R. V. Pound, *Phys. Rev.*, 1946, **69**, 37–38.
53 K. Okamoto, S. Vyawahare and A. Scherer, *J. Opt. Soc. Am. B*, 2006, **23**, 1674.
54 G. M. Akselrod, C. Argyropoulos, T. B. Hoang, C. Ciracì, C. Fang, J. Huang, D. R. Smith and M. H. Mikkelsen, *Nat. Photonics*, 2014, **8**, 835–840.
55 M. D. Leistikow, J. Johansen, A. J. Kettelarij, P. Lodahl and W. L. Vos, *Phys. Rev. B: Condens. Matter Mater. Phys.*, 2009, **79**, 045301.